

1 **Two years of satellite-based carbon dioxide emission quantification at the world's** 2 **largest coal-fired power plants**

3 Daniel H. Cusworth^{1,2}, Andrew K. Thorpe³, Charles E. Miller³, Alana K. Ayasse¹, Ralph Jiorle¹,
4 Riley M. Duren^{1,2,3}, Ray Nassar⁴, Jon-Paul Mastrogiacomo⁵, and Robert R. Nelson³

5 ¹Carbon Mapper, Pasadena, CA, USA

6 ²Arizona Institutes for Resilience, University of Arizona, Tucson, AZ, USA

7 ³Jet Propulsion Laboratory, California Institute of Technology, Pasadena, CA, USA

8 ⁴Environment & Climate Change Canada, Toronto, ON, Canada

9 ⁵University of Toronto, Toronto, ON, Canada

10

11 Corresponding Author: Daniel H. Cusworth (dan@carbonmapper.org)

12

13 **Abstract**

14 Carbon dioxide (CO₂) emissions from combustion sources are uncertain in many places
15 across the globe. Satellites have the ability to detect and quantify emissions from large CO₂ point
16 sources, including coal-fired power plants. In this study, we made observations with the PRecurso
17 IperSpettrale della Missione Applicativa (PRISMA) satellite imaging spectrometer and the Orbiting
18 Carbon Observatory-3 (OCO-3) instrument onboard the International Space Station at over 30 coal-
19 fired power plants routinely between 2021-2022. CO₂ plumes were detected in 50% of acquired
20 PRISMA scenes, which is consistent with the combined influence of viewing parameters on detection
21 (solar illumination, surface reflectance) and unknown factors (like daily operational status). We
22 compare satellite-derived emission rates to *in situ* stack emission observations and find average
23 agreement to within 27% for PRISMA and 30% for OCO-3, though more observations are needed to
24 robustly characterize the error. We highlight two examples of fusing PRISMA with OCO-2 and
25 OCO-3 observations in South Africa and India. For India, we acquired PRISMA and OCO-3

26 observations on the same day and use the high spatial resolution capability of PRISMA (30 m
27 spatial/pixel resolution) to partition relative contributions of two distinct emitting power plants to the
28 net emission. Though an encouraging start, two years of observations from these satellites did not
29 produce sufficient observations to estimate annual average emission rates within low (<15%)
30 uncertainties. However, as the constellation of CO₂-observing satellites is poised to significantly
31 improve in the coming decade, this study offers an approach to leverage multiple observation
32 platforms to better quantify and characterize uncertainty for large anthropogenic emission sources.

33

34 **1 Introduction**

35 Anthropogenic carbon dioxide (CO₂) emissions are dominated by strong discrete point
36 sources: power and other industrial combustion are estimated to make up 59% of global
37 anthropogenic CO₂ emissions with transport, buildings, and other sources making up the remaining
38 20%, 9%, and 12%, respectively (Crippa et al., 2022). Fossil fuel combustion is the largest
39 contributor to warming trends globally since the pre-industrial era (IPCC, 2021). However, there
40 remains uncertainty in the total magnitude of emissions from these sectors as bottom-up emission
41 estimates rely on reported emission factors and activity data, which may vary in granularity and
42 quality across countries and provinces (Hong et al., 2017; Guan et al., 2017). Accurate CO₂ emission
43 quantification is important in light of the Paris Agreement, as participating countries must develop
44 plans and report progress to reduce their country's greenhouse gas (GHG) emissions (UN, 2015).
45 Leveraging atmospheric measurements, particularly satellite remote sensing, can help reduce
46 uncertainty in facility-level CO₂ emission estimates, provided that the observations are accurate and
47 sufficiently sample the facility in time (Hill and Nassar, 2019). Deployed systematically with robust
48 error characterization, this system could be an anchor towards assessing and verifying anticipated

49 CO₂ emission reductions as part of national and global GHG emission reduction plans and
50 agreements.

51 Several studies have shown that atmospheric sounding satellites can accurately quantify some
52 point source CO₂ emissions from large individual coal-fired power plants. First, the Orbiting Carbon
53 Observatory-2 (OCO-2; Crisp et al., 2017) is a space-based instrument that observes solar
54 backscattered near-infrared radiance in the oxygen *A* band (758-772 nm; 0.04 nm spectral resolution),
55 the weak CO₂ band (1594-1619 nm; 0.08 nm spectral resolution), and strong CO₂ band (2042-2082
56 nm; 0.10 nm spectral resolution). OCO-2 views in nadir mode over land, while sun glint mode
57 increases the signal over water giving measurements both land and water, and target mode to target
58 specific validation or calibration sites. With its 10-km wide swath, $\leq 1.3 \times 2.25$ km² pixel resolution,
59 and better than 1.0 ppm precision for retrievals of the column-mean dry-air mole fraction of CO₂
60 (XCO₂) (Taylor et al., 2023), OCO-2 is sensitive to single CO₂ point sources that emit sufficiently
61 close to an OCO-2 orbital track and are spatially isolated from other major CO₂ sources. Using
62 satellite observations from OCO-2, Nassar et al. (2017) detected strong CO₂ enhancements in the
63 near vicinity of seven large coal-fired power plants and employed a Gaussian plume model emission
64 quantification technique to estimate emission rates for these facilities. Further study expanded the set
65 of facilities that could be quantified by OCO-2 (Nassar et al., 2021). Other studies have leveraged
66 the nitrogen dioxide (NO₂) retrieval capability and wide swath of the TROPOspheric Monitoring
67 Instrument (TROPOMI; van Geffen et al., 2020) to attribute and corroborate strong CO₂ signals seen
68 in OCO-2 observations (Hakkarainen et al., 2021; Reuter et al., 2019). The Orbiting Carbon
69 Observatory-3 (OCO-3; Eldering et al., 2019), the flight spare of OCO-2, has been on board the
70 International Space Station (ISS) since May 2019. Like OCO-2, it has been shown capable of
71 quantifying CO₂ power plant emissions. Nassar et al. (2022) analyzed nine successful OCO-3

72 acquisitions of the Bełchatów Power Station and found the variability in satellite-based emission
73 estimates agreed well with the variability in independently reported hourly power generation. Guo et
74 al., (2023) estimated emissions at Chinese power plants using OCO-2/3 and found close agreement
75 with emission inventories. OCO-3 is different than OCO-2 in that it has a two-axis Pointing Mirror
76 Assembly (PMA) for more agile pointing, allowing it to rapidly point off-nadir and take Snapshot
77 Area Mapping (SAM) mode observations over the course of two minutes. These SAMs are
78 approximately 80×80 km² collections of measurements and are typically over sites of interest
79 including cities, power plants, volcanoes, and flux towers.

80 Another class of remote sensing imaging spectrometers – sometimes also referred to as
81 hyperspectral imagers – also have been shown capable of detecting and quantifying strong CO₂
82 signals from large point sources. Thorpe et al. (2017) flew the Next-Generation Airborne/Infrared
83 Imaging Spectrometer (AVIRIS-NG) over a coal-fired power plant in Four Corners, New Mexico,
84 and detected strong CO₂ plumes. AVIRIS-NG observes a large range of solar backscattered radiance
85 (380-2500 nm), but at much coarser spectral resolution (5 nm), and high spatial resolution (e.g., 3 m
86 when flown at 3 km altitude). The much finer spatial resolution of AVIRIS-NG allows for improved
87 visualization of the origin of a CO₂ plume, but at the expense of fine precision for a single observed
88 CO₂ column. Still, Cusworth et al. (2021) analyzed a combination of AVIRIS-NG and the identically
89 built Global Airborne Observatory (GAO) at over 20 power plants in the U.S., quantified emission
90 rates, and found close agreement with continuous emissions monitoring (CEMS) hourly emission
91 observations. From space, the PRecursores IperSpettrale della Missione Applicativa (PRISMA),
92 launched in 2019, like AVIRIS-NG and GAO is sensitive to a large range of solar backscattered
93 radiance (400-2500 nm), albeit at coarser spectral and spatial resolution (10 nm spectral resolution;
94 30 m spatial resolution; Loizzo et al., 2018). PRISMA is a tasked satellite instrument potentially

95 capable of hundreds of $30 \times 30 \text{ km}^2$ observations per day, with equatorial crossing time of 10:30am,
96 and target revisit of seven days, though true revisit depends on tasking priorities of the system.
97 Cusworth et al. (2021) showed a few examples of CO₂ plumes detected and quantified with
98 PRISMA, with quantified emissions similar in magnitude to reported CEMS emissions..

99 The capacity for satellites to be leveraged as useful tools for reducing uncertainty in the global
100 CO₂ anthropogenic emission sector requires synthesis and routine observations (i.e., tasking) of a
101 critical number of facilities. Therefore, in this study, we made observations at a subset of global coal-
102 fired power plants routinely over the course of two years to probe detection limits, emission
103 quantification uncertainty, and data yields. We observed these facilities with both OCO-3 and
104 PRISMA. To our knowledge to date, this study represents the largest satellite-based facility scale
105 investigation of direct CO₂ emission quantification across a diverse set of global power plants, and
106 the first investigation to assess the capability of PRISMA to reliably detect and quantify CO₂ point
107 sources. The results, though not sufficient by themselves to reduce uncertainty relative to bottom-up
108 inventories significantly on an annual basis, show a path forward for data fusion and synthesis of
109 observations from the growing constellation of planned CO₂ sensing satellites.

110

111 **2 Methods**

112 Table 1 lists the locations of all power plants we targeted during this study between 2021-
113 2022 with PRISMA. OCO-3 includes a subset of these sites as well as other fossil fuel combustion
114 sites as part of its list of possible targets. We identified coal-fired power plants to routinely target
115 using a combination of bottom-up and top-down information. Bottom-up coal-fired power plant CO₂
116 emission estimates rely on activity data, that usually includes permitted capacity of a power plant
117 and its operational state; and emission factors, usually estimated from the composition of the coal

118 that is combusted. Inventories, like the Global Energy Monitor (GEM), include this data for a large
 119 set of coal-fired power plants across the globe (GEM, 2023). From the GEM database, we gathered
 120 the top 10 largest bottom-up coal-fired power plants globally. We then gathered a list of top-down
 121 TROPOMI NO₂ combustion hotspots, as inferred by Beirle et al. (2021). We included an additional
 122 seven unique power plants using this dataset. Because the imaging scene size of PRISMA is 30 × 30
 123 km², some adjacent smaller power plants were imaged simultaneously along with these larger power
 124 plants. In total, outside of the U.S., we made PRISMA observations at 27 power plants. In the U.S.,
 125 we chose 10 power plants to routinely target using reported EPA CEMS information
 126 (campd.epa.gov): five of the top 30 emitting power plants, and five progressively lower emitters,
 127 chosen so that we could assess satellite detection capabilities.

128

129 Table 1. Power plants that were targeted specifically by PRISMA in this study.

Power Plant Name	Country	Latitude	Longitude	Number clear-sky observations	Number plume detections	Minimum quantified CO ₂ emission (kt CO ₂ h ⁻¹)	Mean quantified CO ₂ emission (kt CO ₂ h ⁻¹)	Maximum quantified CO ₂ emission (kt CO ₂ h ⁻¹)
Mundra-Adani	India	22.82	69.55	12	7	0.49±0.07	1.09±0.19	1.76±0.32
Korba-Balco	India	22.40	82.74	5	1	NA*	NA	NA
PLN Paiton Baru	Indonesia	-7.71	113.57	4	2	NA	NA	NA
Craig	USA	40.46	-107.59	5	5	0.56±0.11	0.69±0.16	0.8±0.22
Cumberland	USA	36.39	-87.65	1	0	NA	NA	NA
Dry Fork	USA	44.39	-105.46	6	3	0.61±0.09	0.65±0.13	0.69±0.16
H L Spurlock	USA	38.70	-83.82	5	3	1.15±0.32	1.26±0.39	1.37±0.45
Ulsan Hanju (1)	South Korea	35.49	129.33	1	0	NA	NA	NA
Hasdeo	India	22.41	82.69	5	0	NA	NA	NA
Hekinan	Japan	34.83	136.96	6	4	0.72±0.47	3.88±1.09	8.35±2.14
Baotou-1	China	40.66	109.66	5	2	0.19±0.07	0.27±0.07	0.35±0.07
Kendal	South Africa	-26.09	28.97	7	2	0.85±0.13	0.85±0.13	0.85±0.13
NTPC Korba	India	22.39	82.68	6	1	1.28±0.27	1.28±0.27	1.28±0.27

Kriel	South Africa	-26.25	29.18	8	3	0.74±0.15	0.82±0.15	0.95±0.16
Labadie	USA	38.56	-90.84	4	4	0.73±0.18	0.73±0.18	0.73±0.18
Martin Lake	USA	32.26	-94.57	8	8	1.45±0.31	2±0.59	2.6±0.98
Matimba	South Africa	-23.67	27.61	11	8	0.33±0.05	0.72±0.16	1.14±0.32
Matla	South Africa	-26.28	29.14	8	3	0.33±0.05	0.77±0.15	1.37±0.27
Medupi	South Africa	-23.71	27.56	15	12	0.33±0.06	0.83±0.19	1.47±0.34
Mundra-Tata	India	22.82	69.53	12	5	0.38±0.09	0.74±0.13	1.32±0.21
Niederaussem	Germany	51.00	6.67	1	0	NA	NA	NA
Oregon	USA	41.67	-83.44	5	1	NA	NA	NA
Paiton-3	Indonesia	-7.71	113.58	4	4	1.54±0.37	3.16±0.69	4.78±1.02
Rihand	India	24.03	82.79	8	5	0.83±0.17	0.99±0.26	1.36±0.38
Sanfeng	China	40.66	109.76	6	0	NA	NA	NA
Sasan	India	23.98	82.63	9	7	0.65±0.15	1.01±0.24	1.51±0.31
Sooner	USA	36.45	-97.05	6	3	1.05±0.22	1.05±0.22	1.05±0.22
Togtoh	China	40.20	111.36	2	2	0.25±0.06	0.91±0.17	1.58±0.27
Ulsan Hanju (2)	South Korea	35.47	129.38	1	0	NA	NA	NA
Vindhyachal	India	24.10	82.68	9	7	0.33±0.1	0.72±0.15	1.24±0.23
Waigaoqiao	China	31.36	121.60	6	1	NA	NA	NA
Yeosu Hanwha	South Korea	34.84	127.69	2	0	NA	NA	NA
Yosu	South Korea	34.83	127.67	2	0	NA	NA	NA
Al Zour	Kuwait	28.71	48.37	12	0	NA	NA	NA

130 *A value of “NA” indicates that no plumes were detected at this power plant or that the emission quantification
131 algorithm (described in Methods) failed to quantify an emission rate.
132

133 *2.1 PRISMA observations and quantification*

134 PRISMA is a tasked satellite instrument, capable of collecting around 200 30 × 30 km² targets
135 per day and has 20° pointing capability off nadir. Authenticated users can program single observation
136 requests through PRISMA’s web portal (prisma.asi.it), which currently allows for 13 concurrent
137 requests at a time per user. We specified two-week observing windows for each request, and
138 configured requests to collect if the scene-averaged solar zenith angle (SZA) was less than 70° and

139 forecast meteorology anticipated less than 20% cloud cover. If the orbital configuration, weather,
 140 SZA align and there are no other conflicting or higher priority requests, PRISMA images a target.

141 For each acquired PRISMA image, we performed XCO₂ retrievals on all pixels within a 2.5
 142 km radius around the power plant. We retrieve XCO₂ using the Iterative Maximum A Posteriori –
 143 Differential Optical Absorption Spectroscopy (IMAP-DOAS) algorithm, as implemented in
 144 Cusworth et al. (2021). This approach estimates XCO₂ by decomposing an observed radiance
 145 spectrum into high and low frequency features between 1900-2100 nm. For high-frequency features,
 146 we simulate atmospheric transmission of CO₂, H₂O, and N₂O using a Beer-Lambert approximation.
 147 For low-frequency features (e.g., surface reflectance, aerosol scattering), we use an 8-degree
 148 polynomial. The forward model that drives IMAP-DOAS therefore has the following form:

$$149 \quad F^h(\mathbf{x}) = I_0(\lambda) \exp \left(- \sum_{n=1}^6 s_n \sum_{l=1}^{72} A_l \tau_{n,l} \right) \sum_{k=0}^K a_k \lambda^k \quad (1)$$

150 Where F^h is simulated backscattered radiance at wavelength λ , I_0 is incident solar intensity, A_l is the
 151 airmass factor at vertical level $l \in [1,72]$, $\tau_{n,l}$ is the optical depth for each trace gas element, s_n is the
 152 scaling factor applied to the optical depth, and a_k is a polynomial coefficient ($K=8$). Optical depths
 153 are computed by querying meteorological information for pressure and temperature from the
 154 MERRA-2 reanalysis (Gelaro et al., 2017), and using that information to select proper HITRAN
 155 absorption cross sections for each trace gas (Kochanov et al., 2016). To compare the model from
 156 Equation 1 against PRISMA observed radiance (\mathbf{y}), we compute $F^h(\mathbf{x})$ between 1900-2100 nm at
 157 0.02 nm resolution, then convolve the output using the PRISMA full-width half maximum, and
 158 sample at PRISMA wavelength positions. This results in vector $\mathbf{F}(\mathbf{x})$ that is comparable to \mathbf{y} . The
 159 vector \mathbf{x} , also called the state vector, includes scale factors for CO₂, H₂O, N₂O, and polynomial
 160 coefficients: $\mathbf{x} = (s_{CO_2}, s_{H_2O}, s_{N_2O}, a_0, \dots, a_8)$.

161 XCO₂ is retrieved from PRISMA radiance using a Bayesian optimal estimation approach
 162 (Rodgers, 2000). Here, the optimized state vector solution, or posterior, is solved through Gauss-
 163 Newton iteration:

$$164 \quad \mathbf{x}_{i+1} = \mathbf{x}_A + (\mathbf{K}_i^T \mathbf{S}_0^{-1} \mathbf{K}_i + \mathbf{S}_A^{-1})^{-1} \mathbf{K}_i^T \mathbf{S}_0^{-1} [y - \mathbf{F}(\mathbf{x}_i) + \mathbf{K}_i(\mathbf{x}_i - \mathbf{x}_A)] \quad (2)$$

165 Where $\mathbf{S}_0 = [\boldsymbol{\epsilon}\boldsymbol{\epsilon}^T]$ is the observation error covariance matrix defined by the instrument signal to noise
 166 ratio (SNR), \mathbf{x}_A is the prior estimate of the state vector, and \mathbf{S}_A is the prior error covariance matrix.
 167 The matrix \mathbf{K} , or Jacobian matrix, represents the first derivative of the $\mathbf{F}(\mathbf{x})$ with respect to the state
 168 vector:

$$169 \quad \mathbf{K}_i = \left. \frac{\partial \mathbf{F}}{\partial \mathbf{x}} \right|_{\mathbf{x}=\mathbf{x}_i} \quad (3)$$

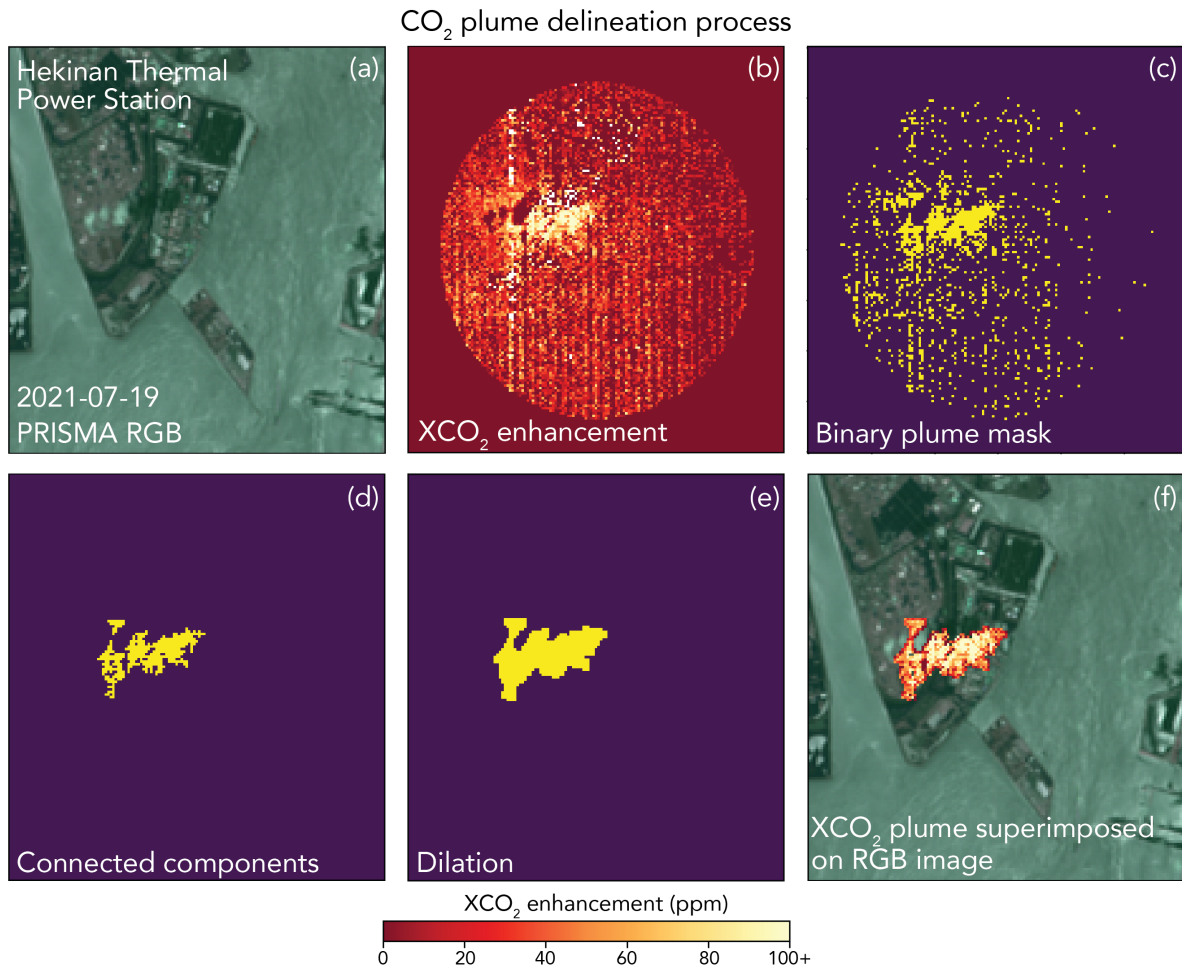
170 The posterior error covariance matrix can be computed explicitly to quantify retrieval precision:

$$171 \quad \hat{\mathbf{S}} = (\mathbf{K}_i^T \mathbf{S}_0^{-1} \mathbf{K}_i + \mathbf{S}_A^{-1})^{-1} \quad (4)$$

172 Across the scenes we acquired with PRISMA, using this retrieval approach, we quantify an
 173 average 3.3 ppm precision for an XCO₂ column. Absolute biases in PRISMA XCO₂ retrievals are
 174 less important for CO₂ plume detection and quantification: systematic retrieval biases are removed
 175 from a scene through the quantification and removal of a local background, as described below. To
 176 characterize bias in emission quantification, we compare emission rates derived from PRISMA to
 177 stack-level CEMS measurements (Section 3.2).

178 We quantified emissions for each PRISMA plume detection using the Integrated Mass
 179 Enhancement (IME) approach (Cusworth et al., 2021). However, we updated the masking scheme
 180 for this analysis to produce more reliable masks for each CO₂ plume. Figure 1 shows the plume
 181 masking procedure for a plume detected at the Hekinan, Japan power plant on July 19, 2021. First,
 182 we apply a background threshold to differentiate candidate plume pixels from the background

183 (method to quantify background threshold described in Section 3.2). We then group enhanced XCO₂
184 pixels into clusters of at least 20 connected pixels. These groups are then buffered with a one-pixel
185 dilation filter to smooth edges and any gaps that exist in a group (Dougherty, 1992). Finally, each
186 cluster is considered part of the plume if at least one of its pixels is within 500 m of an exhaust stack.



187
188 **Figure 1.** Example of the plume delineation and masking process performed on XCO₂ retrievals
189 derived from PRISMA observations. Panel (a) shows the simultaneously observed RGB PRISMA
190 imagery, panel (b) shows retrieved XCO₂ above the background, panels (c)-(e) show the plume
191 masking procedure to isolate enhanced pixels and remove noise, and panel (f) shows the resulting
192 CO₂ plume superimposed on the RGB imagery.

193

194 IME is calculated for a plume using the following equation:

195
$$\text{IME} = \sum_{i=1}^N \Delta\Omega_i \Lambda_i \quad (5)$$

196 where $\Delta\Omega_i$ is the XCO₂ mass enhancement in pixel i relative to background (kg m⁻²), Λ_i is the pixel
197 area (900 m²), and N is the number of pixels in the plume. The CO₂ emission rate Q is estimated from
198 the IME using the following relationship:

199
$$Q = \frac{U_{eff}}{L} \text{IME} \quad (6)$$

200 where $L = \sqrt{\sum_{i=1}^N \Lambda_i}$ is the plume length and U_{eff} is the effective wind speed. The effective wind
201 speed relates IME and plume length parameterizations to true emission rates. This relationship can
202 be empirically estimated through large eddy simulations using the 10-m wind speed (U_{10}). Here we
203 apply the U_{eff} relationship derived from Varon et al., 2018:

204
$$U_{eff} = 1.1 \log U_{10} + 0.6. \quad (7)$$

205 where U_{eff} and U_{10} are in units of [m s⁻¹]. We query the ERA5-Land reanalysis using the Open-Meteo
206 Application Programming Interface (open-meteo.com), which provides hourly wind information
207 globally at 0.1° spatial resolution (Muñoz-Sabater et al., 2021). Uncertainty due to winds is calculated
208 by generating an ensemble of U_{10} values assuming 50% error (Cusworth et al., 2021). Uncertainty
209 due to the CO₂ background is calculated by generating many emission estimates and calculating a
210 standard deviation using an ensemble of background thresholds. Background thresholds are set to
211 vary with scene-averaged CO₂ retrieval precision. Total emission uncertainty is estimated by adding
212 in quadrature the contribution of wind and background uncertainties.

213

214 *2.2 OCO-3 observations and quantification*

215 OCO-3 is also a tasked mission: it can take SAMs over any place of interest within the latitude
216 range of the ISS orbit (about 52° S to 52° N). In addition to the SAM locations we supplied to OCO-
217 3 to overlap with PRISMA targets, there are many other power plant and fossil fuel combustion
218 sources that make up its set of mission targets. However, unlike PRISMA, OCO-3 does not consider
219 cloud forecasts, snow cover, or viewing geometry when planning SAMs and thus the majority of
220 observations fail to produce useful maps of XCO₂. Additionally, aerosol- and albedo-induced XCO₂
221 artifacts are present in many SAMs (Bell et al., 2023) and thus make the detection of plumes even
222 more difficult.

223 For all cloud-free soundings, OCO-3 XCO₂ concentrations are derived using the
224 Atmospheric Carbon Observations from Space (ACOS; O’Dell et al., 2012; Crisp et al., 2012; O’Dell
225 et al., 2018) v10 optimal estimation retrieval, which employs the Levenberg-Marquardt modification
226 of the Gauss-Newton method. In this work, bias corrected XCO₂ from the OCO-3 Lite files is used
227 but the official data quality flag is not applied. This was done because often the quality flag removes
228 XCO₂ retrievals within the plume and makes emission estimation more difficult or impossible
229 (Nassar et al., 2022). For SAMs where we visually identified CO₂ plumes (e.g., Figure 2), emission
230 rates are estimated using two approaches: (1) a Gaussian plume model and (2) the IME method. For
231 the Gaussian plume model approach, we follow the algorithm outlined in Nassar et al. (2022):

232
$$V(x, y) = \frac{Q}{\sqrt{2\pi}\sigma_y(x)u} e^{-\frac{1}{2}\left(\frac{y}{\sigma_y(x)}\right)^2} \quad (8)$$

233
$$\sigma_y(x) = a \cdot \left(\frac{x}{x_0}\right)^{0.894} \quad (9)$$

234 Where V represents the vertical columns within the plume (g/m²), Q is the CO₂ emission rate (g/s),
235 y is the wind direction perpendicular to the plume (m), u is the wind speed at the height of the plume

236 at its midline (m/s) assuming plume rise of 250 m above the stack height, $\sigma_y(x)$ is the standard
237 deviation of the y -direction, x_0 is a characteristic plume length (1000 m), and a is a stability
238 parameter (Nassar et al., 2021). Following Nassar et al. (2022), wind speed and direction inputs are
239 estimated by taking the average of ERA-5 (Bell et al., 2020) and MERRA-2 reanalysis data. The
240 wind direction is optimized by rotating the plume, typically between -30° to 30° away from the mean
241 ERA-5/MERRA-2 direction, and calculating the correlation coefficient (R) of the modeled and
242 observed XCO_2 . The optimized wind direction is the direction that produces the largest R . The
243 background is typically estimated by averaging OCO-3 footprints within a radius of 30 km, excluding
244 the plume itself and a narrow 3 km buffer zone. However, if there are visible artifacts in the XCO_2
245 background that are unrelated to the power plant plume, the background field is modified to avoid
246 them. For example, decreasing the radius of footprints used from 30 km to 20 km. The uncertainty
247 in wind speed is calculated by taking the difference of the emission estimate using two different
248 models (ERA-5 and MERRA2). The background concentration uncertainty is calculated by
249 estimating Q using three different background radii of 30, 40, and 50 km. Q is also calculated for a
250 30 km radius background but only using the left and right halves of the background, relative to the
251 direction of the plume. The standard deviation of both these methods is calculated and the larger of
252 the two is the background uncertainty. The plume rise uncertainty is calculated by estimating Q using
253 plume rise values of 100, 200, 250, 300, and 400 m and taking the standard deviation of those values.
254 Total uncertainty on the emission rate Q using the Gaussian plume method is estimated by adding in
255 quadrature the contribution of wind speed, background concentration, and plume rise uncertainties.

256 To obtain another estimate of emission rate, we also apply an IME quantification approach to
257 the CO_2 plumes, which to our knowledge is the first time the IME method has been applied to OCO-
258 3 SAMS at coal power plants. We first interpolate the XCO_2 retrievals in a SAM to a uniform 2×2

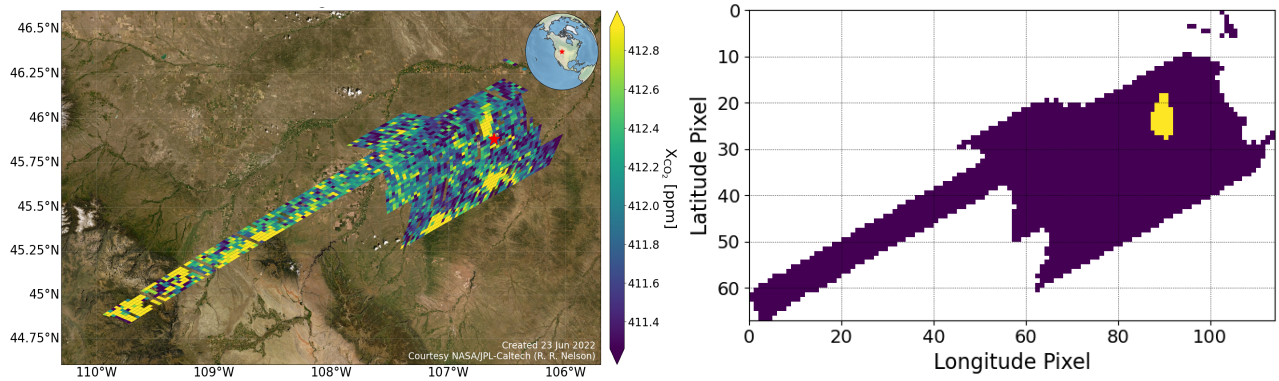
259 km² grid to account for occasional OCO-3 footprint overlap. Similar to Varon et al. (2018), 3 × 3
260 pixel neighborhoods are sampled and the distributions are compared to the background using a
261 Student's *t*-test. The default confidence level for the *t* test is 95% but this is often lowered to visually
262 capture most of the plume. The plume is then smoothed using a 3 × 3 pixel median filter and a
263 Gaussian filter with a standard deviation of 0.5. The U_{eff} calculation is done using an equation
264 approximately equal to Equation 7 ($U_{eff} = 1.0 \log U_{10} + 0.55$). Other recent studies have used various
265 methods (Lin et al., 2023; Brunner et al., 2023), but further research is needed to determine the most
266 accurate way to estimate U_{eff} for an OCO-3-like instrument. The wind direction is the optimized
267 direction determined by the Gaussian plume model. The background XCO₂ estimate is taken from
268 the Gaussian plume model methodology and the plume is typically required to be within 50 km
269 downwind and 8 km crosswind of the source, although these parameters are modified if the plume
270 curves outside of the 8 km crosswind threshold or there are XCO₂ artifacts that should be avoided.

271 The uncertainty for the IME method is estimated similarly to the Gaussian plume model
272 method. The uncertainty in wind speed is calculated by taking the standard deviation of the emission
273 estimates using wind speed from two different models (ERA-5 and MERRA2). The background
274 concentration uncertainty is calculated by estimating Q using the different backgrounds calculated in
275 the Gaussian plume model method: a 20 km radius, 30 km radius, 40 km radius, left half, full circle,
276 and right half. The standard deviation of the three radii estimates and left half, full circle, and right
277 half estimates are calculated and the larger of the two is the background uncertainty. Uncertainty of
278 the Student's *t*-test confidence level is also estimated. The confidence level and -10% and +10% of
279 the confidence level are used to find Q . For example, if the confidence level needed to visually
280 capture the XCO₂ plume is 85%, Q is calculated for 75%, 85%, and 95% and the standard deviation
281 of those three values represents the confidence level uncertainty. Total uncertainty on the emission

282 rate Q using the IME method is estimated by adding in quadrature the contribution of wind speed,
283 background concentration, and Student's t -test confidence level uncertainties.

284 Figure 2 shows IME methodology successfully identifying an XCO₂ plume from an OCO-3
285 SAM taken over the Colstrip power plant.

286



287

288 **Figure 2.** IME plume identification approach applied to an example OCO-3 SAM at the Colstrip
289 power plant on 18 August 2021. Left panel: OCO-3 SAM bias corrected XCO₂. Right panel: yellow
290 pixels indicate the final plume mask.

291

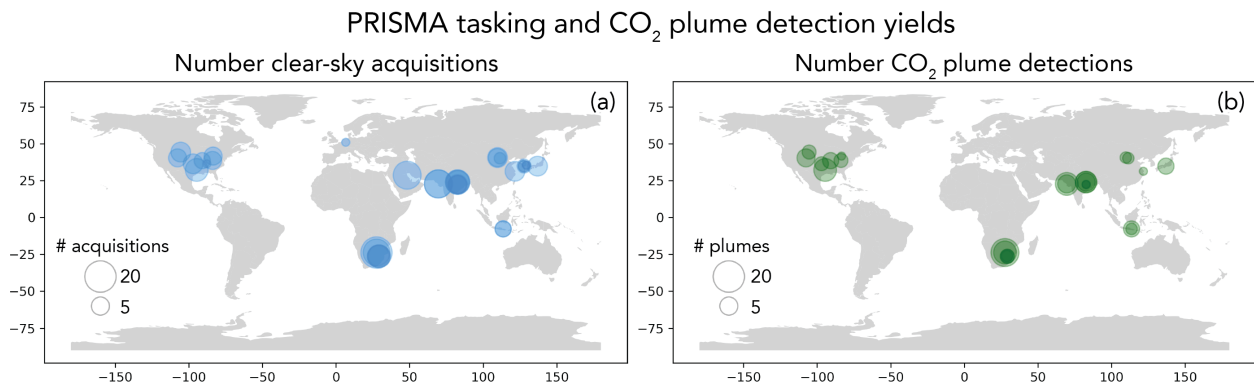
292 **3 Results**

293 *3.1 Global yields from two years of observations*

294 Figure 3a shows a global map of power plants we targeted with PRISMA, with the marker
295 for each power plant's location (latitude, longitude) scaled to represent the number of successful
296 acquisitions between 2021-2022. In total, we acquired 181 PRISMA images, which corresponds to
297 314 unique power plant observation scenes. Of these scenes, 210 were of sufficient quality to attempt
298 CO₂ retrieval and plume detection, with quality mostly determined by visual inspection for clouds
299 and haze. Of these 210 scenes, 104 were determined to have CO₂ plumes (Figure 3b). Scenes were

300 marked as containing CO₂ plumes through inspection of XCO₂ and visible imagery: if a large cluster
301 of pixels with elevated XCO₂ above the background were also in the vicinity of a power plant exhaust
302 stack, an analyst would mark the scene as containing a CO₂ plume. Routine tasking observations with
303 PRISMA resulted in an average of 6 acquisitions for each power plant (maximum 15), roughly one
304 image acquired per quarter. Of these acquisitions, plumes were detected on average four times per
305 facility (maximum 12).

306 For OCO-3, 1363 power plant SAMs were taken during September 2019 to December 2022.
307 Of these, 139 XCO₂ plumes emanating from power plants were visually identified. However, only
308 14 were for power plants that were also observed by PRISMA and have CEMS validation (nine
309 Colstrip cases, two Martin Lake cases, and three Craig cases). The acquisition rates are low relative
310 to PRISMA because OCO-3 does not account for scene favorability when planning its SAMs. For
311 example, OCO-3 took 66 Colstrip SAMs from 2019-2022 yet only yielded nine high-quality XCO₂
312 plume cases.

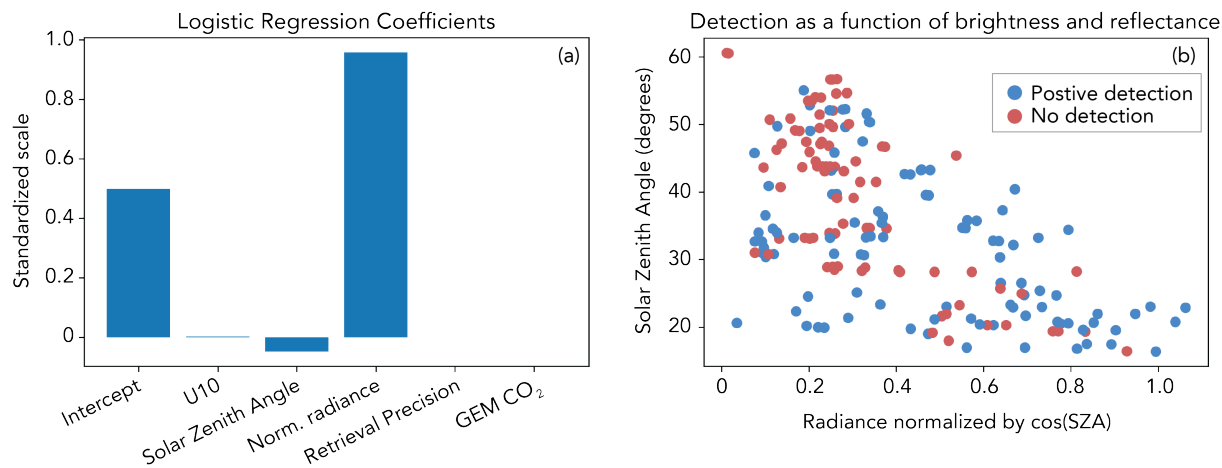


313
314 **Figure 3.** Data yields from PRISMA continually between 2021-2022. Panel (a) shows the number
315 of clear-sky acquisitions for each power plant. Panel (b) shows the number of plumes detected by an
316 analyst for each of the observed power plants.

317

318 The low observed average detection rate of CO₂ plumes is a result of three primary factors:
319 (1) observing conditions at each facility including solar zenith angle (SZA) and surface reflectance;
320 (2) local meteorology; and (3) operational status at each power plant at the time of acquisition. To
321 test how well these factors predict the presence of a plume for PRISMA, we fit a logistic regression
322 classification function with a sparse (L1) penalty to our dataset (Fan et al., 2008). This algorithm fits
323 a logit function to the plume detection outcome of each scenes (i.e., detected plume = TRUE, no
324 detected plume = FALSE) using a set of predictor variables that are likely candidates to explain
325 prediction results. In this setup, the statistical model is fit using the following predictor variables –
326 SZA, U_{10} , average single-sounding retrieval precision across the scene, annual bottom-up emission
327 estimate for the power plant using GEM, and average observed radiance between 1900-2100 nm
328 within the scene normalized by the cosine of the SZA. This last factor is a simple proxy for surface
329 reflectance, although it does not take into account other factors that influence radiance observations
330 (e.g., water vapor, aerosols, other atmospheric constituents). We split the data so that 50% was used
331 to train the model and 50% was reserved as a test set. The predictor variables were all standardized
332 by their mean and standard deviation before the model was fit. The results of classification can be
333 summarized using two statistics: precision (ratio of true positives to sum of true positives and false
334 positives) and recall (ratio of true positives to sum of true positives and false negatives). The results
335 of fitting a logistic regression model to the data show minor prediction performance, with precision
336 = 0.60 and recall = 0.69 for positive plume detection. The regression coefficients are shown in Figure
337 4a. The coefficient with the highest weight is normalized radiance. Figure 4b shows SZA against
338 normalized radiance, with red dots indicating no plume detection and blue dots representing positive
339 plume detection. Though no clear separation exists, there is a cluster of no plume detection at high
340 SZA and low normalized radiance. This is a consistent and expected relationship, as SZA and surface

341 reflectance are principal drivers of the quantity of light that is observed by the satellite, and therefore
342 SNR of the observation.
343



344
345 **Figure 4.** CO₂ plume prediction using various atmospheric, retrieval, and bottom-up information.
346 Panel (a) shows the results of fitting a logistic regression classification model to the set of PRISMA
347 acquisitions where an analyst identified the presence or lack of a plume. Panel (b) shows the top two
348 explanatory variables (SZA and normalized radiance) along with plume classification.

349
350 The logistic regression model performed better on the test data set than predictions made at
351 random, though the prediction performance was still low. Missing from the model is sub-annually
352 resolved information regarding operating status. For most of the power plants outside the U.S., we
353 do not have information on daily operations of a power plant. In many cases of non-detects, we could
354 simply be observing a power plant temporarily not in operation. Another possibility is that at the time
355 of acquisition, some power plants were operating at reduced capacity, meaning that CO₂ emission
356 rates were lower than those predicted by annual emission factors or activity data. If the true CO₂
357 emission rate was below the minimum detection limit (MDL) possible by the PRISMA satellite, then

358 it would show as a non-detect. However, even if the emission were near or slightly above the
359 PRISMA MDL, the probability of detection would still be low as slight variations in atmospheric
360 properties, as seen in Figure 4, would then influence the ability to detection a CO₂ plume.

361

362 *3.2 Validation of PRISMA and OCO-3 emission rates against CEMS*

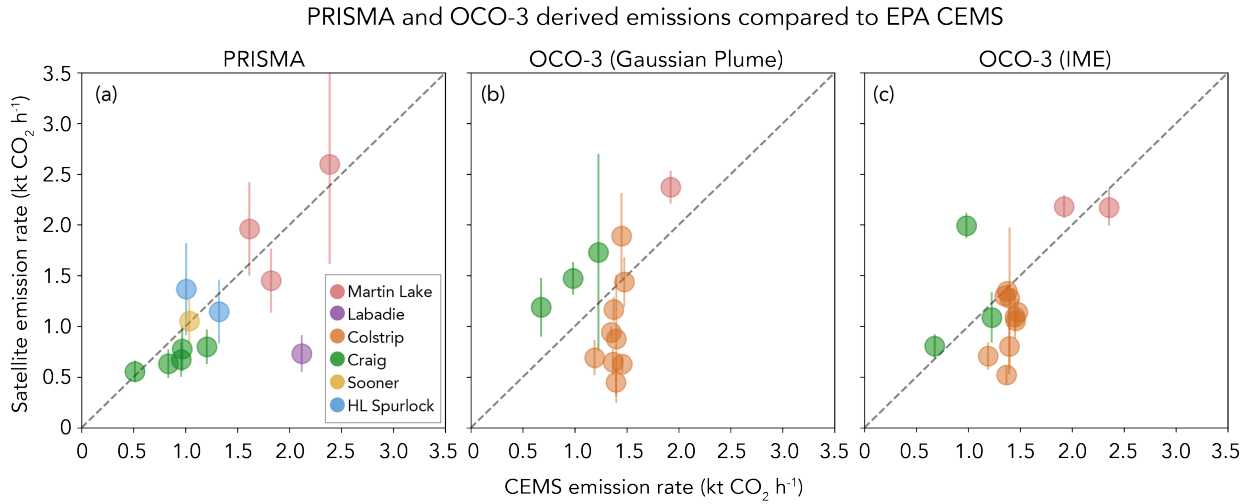
363 For each power plant where a CO₂ plume was identified, we quantify emissions using the
364 IME approach described by Equations 5-7. In order to estimate the XCO₂ mass enhancement ($\Delta\Omega$ in
365 Equation 1), a local background must be quantified and subtracted from total XCO₂ retrievals across
366 the scene. To do this, we apply a concentration threshold β to initiate the plume masking and
367 segmentation process (described in Methods section). Once we have a plume mask, we apply another
368 concentration threshold γ to the remaining XCO₂ pixels that exist outside of the plume. This value γ
369 represents the XCO₂ background that we use to calculate the XCO₂ enhancement that is used in the
370 IME formulation of Equation 1. Thresholds β and γ largely influence the magnitude of the emission
371 rate and are not known a priori. For global generalizability, we wish to estimate β and γ such that
372 they do not vary across power plants, seasons, regions, etc. Therefore, we parameterize β and γ as
373 percentiles under the assumption that the local contrast between enhanced CO₂ plume pixels and the
374 background should be similar across PRISMA scenes.

375 To estimate values for β and γ , we compare EPA CEMS data for power plants in the U.S.
376 with estimated emission rates from PRISMA. In total, we have 12 scenes in the U.S. with CEMS
377 information that pertain to 5 power plants. We then optimize β and γ such that the output of an
378 ordinary least squares regression produces a slope near unity. Figure 5a shows the results of this
379 optimization which produces an optimal β percentile of 94% and a γ percentile of 62%. The results
380 also show decent correlation between CEMS data and PRISMA-derived emission rates ($R^2 = 0.43$).

381 A single outlier at the Labadie power plant (imaged July 10, 2022) shows the largest discrepancy
382 from CEMS data (69%), but the remaining plumes show average 27% relative difference from CEMS
383 data. If we remove the one data point at Labadie, the R^2 improves to 0.75. Though a limited sample
384 size, between PRISMA and OCO-3, these scenes represent variability in solar geometries (20-40°
385 SZA), surface reflectance (0.09-0.90 normalized radiance), and reported emission rates (0.51 – 2.39
386 kt CO₂ h⁻¹). Therefore, we use these optimal parameters and apply them to our global dataset of
387 PRISMA detections. These emission rates are reported in Table 1. There are some instances when
388 performing IME emission calculations using these thresholds and plume masking technique do not
389 result in emission rates (e.g., the plume masking procedure produces a mask with no pixels). In these
390 cases, we report a detection but not an emission quantification.

391 Figures 5b and 5c shows the comparison between OCO-3 and CEMS at some power plants
392 that overlap with PRISMA observations (14 scenes total). OCO-3 Gaussian plume model emission
393 rates (Fig. 5b) have an improved correlation compared to PRISMA ($R^2 = 0.51$), although with greater
394 bias (average 47% relative difference from CEMS). The OCO-3 IME estimates (Fig. 5c) have worse
395 R^2 (0.32) but a better RMSE (0.45 kt CO₂/hr) compared to the Gaussian plume model estimates (0.84
396 kt CO₂/hr), with 9 of the 14 cases being within 30% of the reported CEMS emission and an average
397 relative difference of 30% for all 14 cases. Additionally, the least squares fit for IME is closer to the
398 1-to-1 line than for the Gaussian plume model.

399



400

401 **Figure 5.** Comparison of emission rates in the U.S. between satellite-derived estimates and CEMS
 402 information. Panel (a) shows a comparison between PRISMA derived emission rates and CEMS (R^2
 403 = 0.43), panel (b) shows a comparison between OCO-3 and CEMS using the Gaussian plume model
 404 ($R^2 = 0.51$), and panel (c) shows a comparison between OCO-3 and CEMS using IME ($R^2 = 0.32$).

405

406 Unique sources of error for OCO-3 emission estimates include geolocation errors in the
 407 XCO₂ product. These errors are typically less than 1 km, but can be up to 2 km (Taylor et al., 2023).
 408 Errors of this magnitude, about the size of an OCO-3 footprint ($\sim 2 \times 2$ km²), may mean that an entire
 409 footprint is not included when estimating emissions using the Gaussian plume method, which
 410 assumes that the plume only extends downwind of the known source location. The Gaussian plume
 411 model is also susceptible to wind direction errors, and requires the plume to be Gaussian in shape,
 412 which is often not true. IME, while not suffering from wind direction or geolocation-induced errors,
 413 assumes that the entire plume is captured in a given SAM, which is sometimes not true and results in
 414 an underestimation of emissions. IME is also sensitive to errors in U_{eff} parameterization.

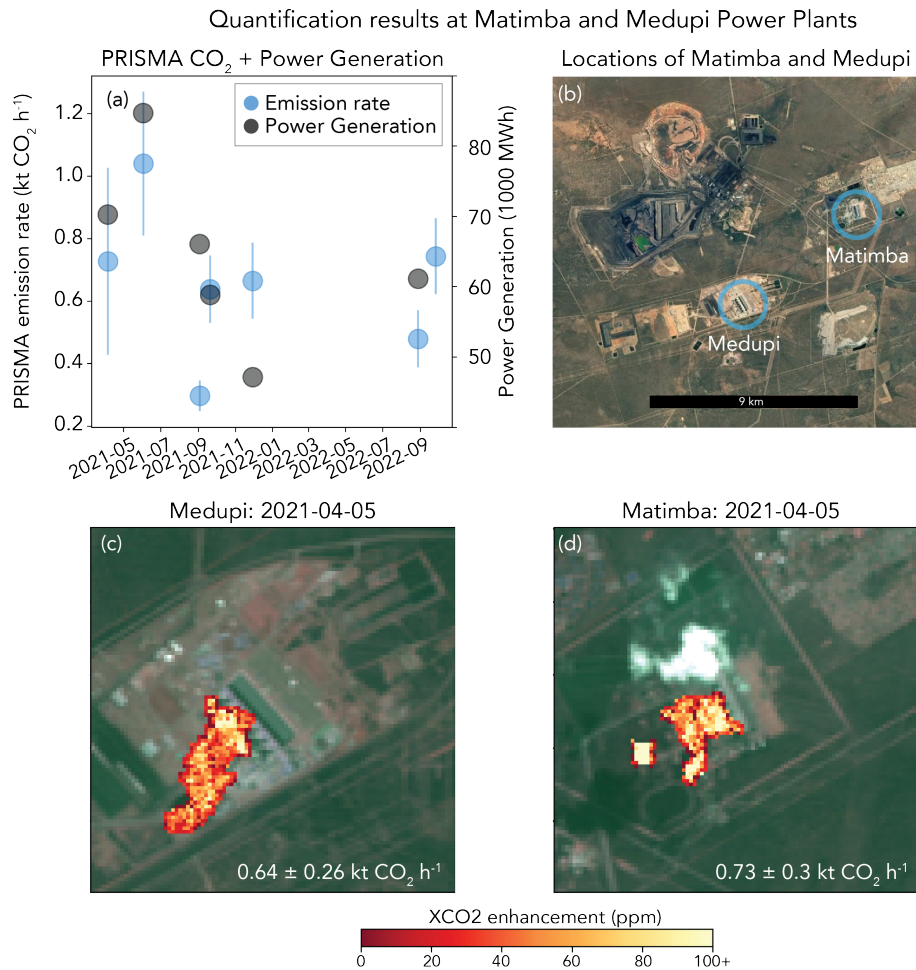
415

416 *3.3 Comparison and fusion of PRISMA and OCO*

417 Outside the U.S., PRISMA observed the Matimba power station in South Africa 11 times and
418 quantified emission rates 7 times. Emissions from Matimba have previously been quantified and
419 validated using OCO-2 (Hakkarainen et al., 2021). This station does not report hourly emission rates,
420 but does report daily power generation (Eskom, 2023). Though not a direct comparison, we can use
421 this information to check if the emission quantification approach we describe above captures some
422 variability in activity at this power plant. Figure 6a shows the emission rates we quantified compared
423 against reported power generation. We see rough agreement in variability – the high power
424 generation reported between Apr to July 2021 (70000-85000 MWh) drop for subsequent dates
425 (47000-66000 MWh) between Sep 2021 to Sep 2022, a drop which is also seen in the PRISMA-
426 derived CO₂ emission rate. Across all observations, we estimate an emission rate range of 0.30-1.04
427 kt CO₂ h⁻¹ (average 0.66 kt CO₂ h⁻¹). This average emission rate is substantially lower than the
428 average 2.50 kt CO₂ h⁻¹ emission rate estimated from OCO-2 and TROPOMI between 2018-2020,
429 but within the range of emissions estimates directly quantified with OCO-2 (0.30-7.20 kt CO₂ h⁻¹;
430 Hakkarainen et al., 2021). However, this discrepancy could be result of (1) changes in activity or
431 variability or (2) existence of other nearby emission sources. For changes in activity, during August
432 2020, the Matimba reported a large range of power generation (65000-94000 MWh) and emission
433 estimates derived directly from OCO-2 were also highly variable (0.88-4.33 kt CO₂ h⁻¹). Given that
434 maximum power generation at the time of a PRISMA observation was 85000 MWh, some of the
435 discrepancy in maximum CO₂ quantification between PRISMA and OCO-2 could be due to activity.

436 Nearby (7 km) the Matimba Power Station is the Medupi Power Plant (Figure 6b). Figure 6c
437 show the Medupi CO₂ plume observed during the same PRISMA overpass on Apr 5, 2021. The
438 PRISMA derived emission rate for Medupi is 0.64 ± 0.26 kt CO₂ h⁻¹ and for Matimba is 0.73 ± 0.30

439 kt CO₂ h⁻¹. Given the proximity of the two power plants, the higher derived emission rate reported
 440 for Matimba from previous studies could actually be a result of a net emission from these two
 441 facilities. The OCO-2 flight track is located tens of kilometers downwind from Matimba and Medupi,
 442 making a clear delineation between potentially co-emitted distinct emission plumes near impossible.
 443 If we sum emission rates from both Medupi and Matimba, we quantify a range of 0.89-1.73 kt CO₂
 444 h⁻¹ (1.30 ± 0.28 kt CO₂ h⁻¹), which is still lower, but closer to the average emissions quantified by
 445 OCO-2.



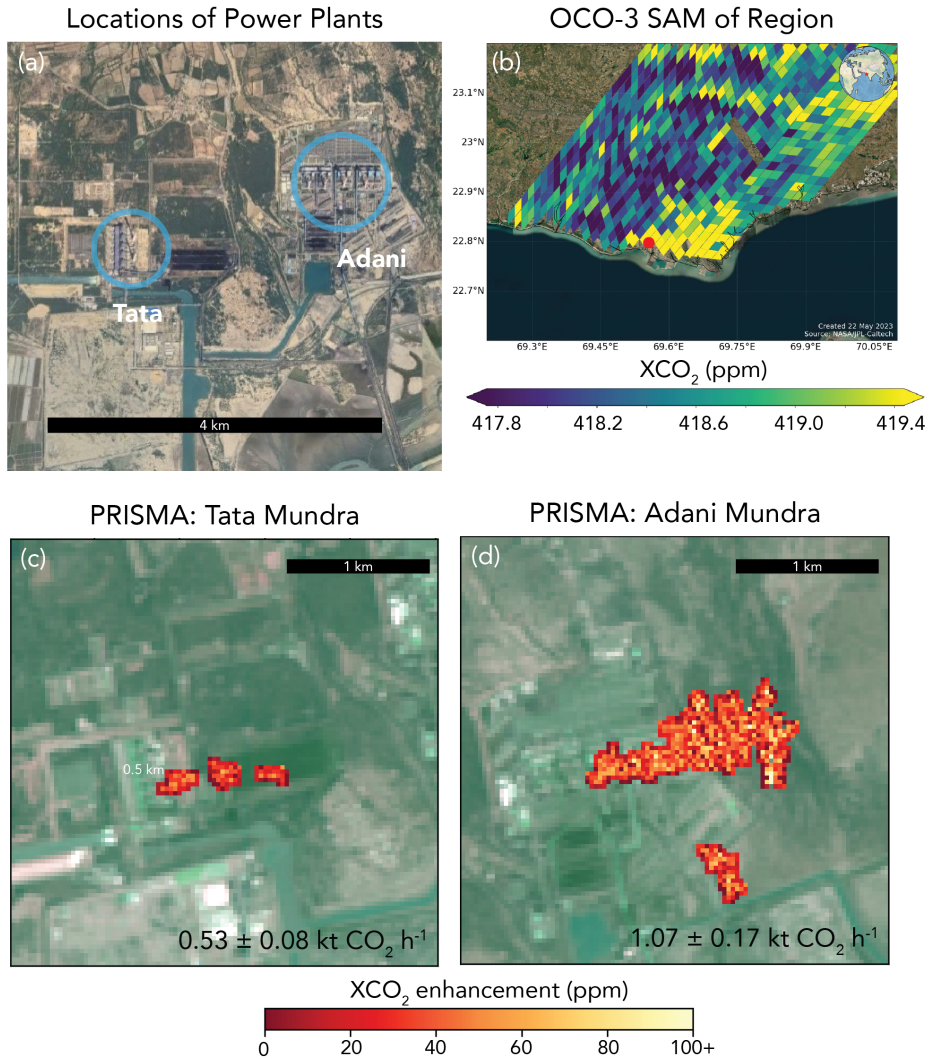
446
 447 **Figure 6.** Emission rates and reported power generation at the Matimba and Medupi power plants in
 448 South Africa. Panel (a) shows the CO₂ emission rates derived from PRISMA and the reported daily

449 power generation for the day of PRISMA overpass. Panel (b) shows the locations of the Medupi and
450 Matimba power plants (base imagery provided by Google Earth; © Google Earth 2023). Panels (c)
451 and (d) show plume imagery and emission rates for a PRISMA overpass on Apr 5, 2021.

452
453 The ability to differentiate the contribution of unique point sources to a regional total is an
454 application made possible by joint observing of imaging spectrometers and atmospheric sounders.
455 Figure 7 shows observations that were made at the Tata Mundra Ultra Mega Power Plant and the
456 Adani Mundra Thermal Power Project: two power plants less than 3 km apart. Both OCO-3 and
457 PRISMA imaged the power plants on Apr 9, 2022. Figure 7b shows the OCO-3 SAM (taken 04:41
458 UTC) – large CO₂ enhancements appear along the coastline likely associated with emission from
459 these power plants. PRISMA imaged the power plants less than two hours later (06:02 UTC) and
460 detected CO₂ plumes at each facility (Figure 7b-c). The OCO-3 derived emission rate using Gaussian
461 plume approaches is 5.5 ± 0.7 kt CO₂ h⁻¹, but the emission rate derived using the IME approach is
462 much lower (3.0 kt CO₂ h⁻¹). For this case, the IME approach may be more appropriate as the shape
463 of the OCO-3 plume (Figure 7b) is more diffuse in nature and does not visibly resemble a Gaussian
464 structure. The PRISMA emission rate for the Adani plant is 1.07 ± 0.17 kt CO₂ h⁻¹ and for the Tata
465 Mundra plant is 0.53 ± 0.08 kt CO₂ h⁻¹. We can use this information to estimate that 67% of the net
466 CO₂ emission came from Adani, and the remaining 33% came from the Tata plant. The combined
467 emission rate (1.60 ± 0.25 kt CO₂ h⁻¹) is lower than the OCO-3 IME emission rate. Like the Matimba
468 power plant, some of this discrepancy may partially be explained by bias or uncertainty in retrievals,
469 background, and wind information. Also, lower estimates of CO₂ emissions from PRISMA are
470 consistent with the fact that PRISMA is only sensitive to emissions at two exhaust stacks, while the
471 OCO-3 observation includes all CO₂ sources in the industrial area around Mundra. Continued

472 validation of retrieved emission rates against ground standards (e.g., CEMS) will help better quantify
473 bias and uncertainty. However, even with lingering uncertainty, the near simultaneous observations
474 of OCO-3 and PRISMA can help us disentangle the relative contributions from each power plant.
475

Near-simultaneous OCO-3 & PRISMA observations (2022-04-09)



476
477 **Figure 7.** Near-simultaneous observation of two power plants in Mundra, India on Apr 9, 2022. Panel
478 (a) shows the locations of two power plants spaced less than 3 km apart: Tata Mundra and Adani
479 Mundra Power Stations (base imagery provided by Google Earth; © Google Earth 2023). Panel (b)

480 shows the OCO-3 SAM with a red dot showing the location of the power plants. Panel (c) and (d)
481 show the PRISMA acquisition (less than 2 hours after OCO-3) over the two power plants with
482 associated emission rates.

483

484 **Conclusion**

485 We observed a global set of power plants for two years between 2021-2022 with both
486 PRISMA and OCO-3 to test the ability of these satellite platforms to do routine operational
487 monitoring of CO₂ emissions. When PRISMA observations were of sufficient quality to perform
488 XCO₂ retrievals, we detected CO₂ plumes nearly half of the time. We fit a logistic regression
489 classification using plume detections and find that there is some relationship between SZA and
490 surface reflectance that partially explains plume prediction; consistent given that these factors are
491 major drivers of SNR. The remaining non-plume detections may be due to operational status of a
492 power plant at the time of observation. We compared emission rates from both PRISMA and OCO-
493 3 to power plants in the U.S. where we have access to hourly *in situ* CEMS emission information.
494 We find significant correlation between satellite and *in situ* estimates, though some significant biases
495 may exist for some of the observations for both PRISMA and OCO-3. Also, the quantity of CEMS
496 observations was limited (~10 for each instrument), so robust calibration is not yet possible. Still,
497 early results show that under the right conditions, satellites can provide reliable estimates of CO₂
498 emissions at discrete point source locations. This is consistent with the close agreement between
499 airborne imaging spectrometer emissions and CEMS information (Cusworth et al., 2021).

500 Fusion of information from atmospheric sounders like OCO-3 and imaging spectrometers
501 like PRISMA is valuable for cross-validation and source attribution. We see this particularly for our
502 examples at the Matimba and Medupi power plants in South Africa and the Tata and Adani power

503 plants in Mundra, India. In these cases, and particularly at Mundra where near-simultaneous
504 PRISMA and OCO-3 observations were taken, OCO-2/3 provides a local, but coarse resolution
505 emission constraint for a complex of facilities that emit large CO₂ quantities. PRISMA, with its 30
506 m pixel resolution, then can help refine relative contributions of single emitters against the net
507 emission flux. More work is needed to refine cross-validation between instruments, but initial
508 observation shows one avenue for data from multiple observing systems to be complementary
509 aggregated and analyzed.

510 Even when combining information from both satellites, there is still too little sampling to
511 constrain facility emissions within low uncertainties. Cusworth et al. (2021), using arguments from
512 Hill and Nassar (2019), suggested that nearly 30 unbiased observations from a PRISMA-class
513 instrument is needed per year at each power plant to reduce annual uncertainties below 14% (i.e.,
514 reduce emission uncertainty from Non-Annex I countries below 1 Gt CO₂ per year). No power plant
515 in this study met this minimum sampling requirement. However, there will be a significant increase
516 in data volumes and observation performance of satellite remote sensing capabilities for CO₂, from
517 both recently launched and planned imaging spectrometers including EMIT (launched 2022; Thorpe
518 et al., in revision); EnMAP (launched 2022; Guanter et al., 2015); Carbon Mapper/Tanager 1-2
519 (Planned launch 2024; Duren et al., 2021), and atmospheric sounders including CO2M (Sierk et al.,
520 2019). Improved observation of global power plants and emission quantification with robust error
521 characterization will be vital to reduce global uncertainty of anthropogenic emissions from fossil fuel
522 combustion sources.

523

524 **Data Availability.**

525 The OCO-3 XCO₂ and other retrieval properties are publicly available at the NASA Goddard Earth
526 Science Data and Information Services Center (GES-DISC). The full suite of retrieval products in
527 the standard per-orbit format can be obtained at OCO Science Team et al., 2021,
528 <https://doi.org/10.5067/D9S8ZCHCADE>. The lightweight per-day format data (Lite files), which
529 includes the bias corrected estimates of XCO₂, can be obtained at OCO Science Team et al., 2022,
530 <https://doi.org/10.5067/970BCC4DHH24>. PRISMA data including radiance for each scene and
531 XCO₂ retrievals is available at <https://doi.org/10.5281/zenodo.8083596>.

532

533 **Acknowledgments.** This work was supported by the Orbiting Carbon Observatory Science Team.
534 We thank the Italian Space Agency for the PRISMA satellite targets. Portions of this work were
535 undertaken at the Jet Propulsion Laboratory, California Institute of Technology, under contract with
536 NASA.

537

538 **Author Contributions.** DHC designed the study. DHC, AKA, RJ tasked and acquired PRISMA
539 data. DHC performed PRISMA emission quantification and validation. RRN performed OCO-3
540 quantification and validation. RN and JPM helped implement OCO-3 quantification algorithms. All
541 authors provided feedback on results and the manuscript.

542

543

544 **Competing interests.** The authors declare no conflicts of interest.

545

546 **References**

547 Beirle, S., Borger, C., Dörner, S., Eskes, H., Kumar, V., de Laat, A. and Wagner, T., 2021. Catalog
548 of NO_x emissions from point sources as derived from the divergence of the NO₂ flux for
549 TROPOMI. *Earth System Science Data*, 13(6), pp.2995-3012. DOI [https://doi.org/10.5194/essd-13-](https://doi.org/10.5194/essd-13-2995-2021)
550 2995-2021

551

552 Bell, B., Hersbach, H., Berrisford, P., Dahlgren, P., Horányi, A., Sabater, M., et al.
553 (2020). ERA5 hourly data on pressure levels from 1950 to 1978 (preliminary
554 version). Copernic. Clim. Change Serv. (C3S) Clim. Data Store (CDS). AvailableAt:
555 [https://cds.climate.copernicus-climate.eu/cdsapp#!/dataset/reanalysis-era5-](https://cds.climate.copernicus-climate.eu/cdsapp#!/dataset/reanalysis-era5-pressure-levels-preliminary-back-extension?tab=overview)
556 [pressure-levels-preliminary-back-extension?tab=overview.](https://cds.climate.copernicus-climate.eu/cdsapp#!/dataset/reanalysis-era5-pressure-levels-preliminary-back-extension?tab=overview)

557

558 Bell, E., O'Dell, C.W., Taylor, T.E., Merrelli, A., Nelson, R.R., Kiel, M., Eldering, A., Rosenberg,
559 R. and Fisher, B., 2023. Exploring bias in the OCO-3 snapshot area mapping mode via geometry,
560 surface, and aerosol effects. *Atmospheric Measurement Techniques*, 16(1), pp.109-133. DOI
561 <https://doi.org/10.5194/amt-16-109-2023>

562

563 Brunner, D., Kuhlmann, G., Henne, S., Koene, E., Kern, B., Wolff, S., Voigt, C., Jöckel, P.,
564 Kiemle, C., Roiger, A. and Fiehn, A., 2023. Evaluation of simulated CO₂ power plant plumes from
565 six high-resolution atmospheric transport models. *Atmospheric Chemistry and Physics*, 23(4),
566 pp.2699-2728. DOI <https://doi.org/10.5194/acp-23-2699-2023>

567

568 Crippa, M., Guizzardi, D., Banja, M., Solazzo, E., Muntean, M., Schaaf, E., Pagani, F., Monforti-
569 Ferrario, F., Olivier, J., Quadrelli, R., Risquez Martin, A., Taghavi-Moharamli, P., Grassi, G.,

570 Rossi, S., Jacome Felix Oom, D., Branco, A., San-Miguel-Ayanz, J. and Vignati, E., CO2
571 emissions of all world countries - 2022 Report, EUR 31182 EN, Publications Office of the
572 European Union, Luxembourg, 2022, [doi:10.2760/730164](https://doi.org/10.2760/730164), JRC130363

573 Crisp, D., Fisher, B.M., O'Dell, C., Frankenberg, C., Basilio, R., Bösch, H., Brown, L.R., Castano,
574 R., Connor, B., Deutscher, N.M. and Eldering, A., 2012. The ACOS CO2 retrieval algorithm—part
575 II: global XCO2 data characterization. *Atmospheric Measurement Techniques*, 5(4), pp.687-707.
576 DOI <https://doi.org/10.5194/amt-5-687-2012>

577

578 Cusworth, D.H., Duren, R.M., Thorpe, A.K., Eastwood, M.L., Green, R.O., Dennison, P.E.,
579 Frankenberg, C., Heckler, J.W., Asner, G.P. and Miller, C.E., 2021. Quantifying global power plant
580 carbon dioxide emissions with imaging spectroscopy. *AGU Advances*, 2(2), p.e2020AV000350.
581 DOI <https://doi.org/10.1029/2020AV000350>

582

583 Dougherty, E.R., 1992. An introduction to morphological image processing. In *SPIE. Optical*
584 *Engineering Press*.

585

586 Duren, R., Cusworth, D., Ayasse, A., Herner, J., Thorpe, A., Falk, M., Heckler, J., Guido, J.,
587 Giuliano, P., Chapman, J. and Green, R., 2021, December. Carbon Mapper: on-orbit performance
588 predictions and airborne prototyping. In *AGU Fall Meeting Abstracts (Vol. 2021, pp. A53F-05)*.

589

590 Eldering, A., Taylor, T.E., O'Dell, C.W. and Pavlick, R., 2019. The OCO-3 mission: measurement
591 objectives and expected performance based on 1 year of simulated data. *Atmospheric Measurement*
592 *Techniques*, 12(4), pp.2341-2370. DOI <https://doi.org/10.5194/amt-12-2341-2019>

593

594 Fan, R.E., Chang, K.W., Hsieh, C.J., Wang, X.R. and Lin, C.J., 2008. LIBLINEAR: A library for
595 large linear classification. *the Journal of machine Learning research*, 9, pp.1871-1874. DOI
596 <https://doi.org/10.5555/1390681.1442794>

597

598 Gelaro, R., McCarty, W., Suárez, M.J., Todling, R., Molod, A., Takacs, L., Randles, C.A.,
599 Darmenov, A., Bosilovich, M.G., Reichle, R. and Wargan, K., 2017. The modern-era retrospective
600 analysis for research and applications, version 2 (MERRA-2). *Journal of climate*, 30(14), pp.5419-
601 5454. <https://doi.org/10.1175/JCLI-D-16-0758.1>

602

603 GEM, Global Energy Monitor's Global Coal Plant Tracker, URL
604 <https://globalenergymonitor.org/projects/global-coal-plant-tracker/tracker/>, last accessed May 24,
605 2023

606

607 Guan, D., Liu, Z., Geng, Y., Lindner, S. and Hubacek, K., 2012. The gigatonne gap in China's
608 carbon dioxide inventories. *Nature Climate Change*, 2(9), pp.672-675. DOI
609 <https://doi.org/10.1038/nclimate1560>

610

611 Guanter, L., Kaufmann, H., Segl, K., Foerster, S., Rogass, C., Chabrillat, S., Kuester, T., Hollstein,
612 A., Rossner, G., Chlebek, C. and Straif, C., 2015. The EnMAP spaceborne imaging spectroscopy
613 mission for earth observation. *Remote Sensing*, 7(7), pp.8830-8857. DOI
614 <https://doi.org/10.3390/rs70708830>

615

616 Guo, W., Shi, Y., Liu, Y. and Su, M., 2023. CO2 emissions retrieval from coal-fired power plants
617 based on OCO-2/3 satellite observations and a Gaussian plume model. *Journal of Cleaner*
618 *Production*, 397, p.136525. DOI <https://doi.org/10.1016/j.jclepro.2023.136525>
619

620 Hakkarainen, J., Szelağ, M.E., Ialongo, I., Retscher, C., Oda, T. and Crisp, D., 2021. Analyzing
621 nitrogen oxides to carbon dioxide emission ratios from space: A case study of Matimba Power
622 Station in South Africa. *Atmospheric Environment: X*, 10, p.100110. DOI
623 <https://doi.org/10.1016/j.aeaoa.2021.100110>
624

625 Hill, T. and Nassar, R., 2019. Pixel size and revisit rate requirements for monitoring power plant
626 CO2 emissions from space. *Remote Sensing*, 11(13), p.1608. DOI
627 <https://doi.org/10.3390/rs11131608>
628

629 Hong, C., Zhang, Q., He, K., Guan, D., Li, M., Liu, F. and Zheng, B., 2017. Variations of China's
630 emission estimates: response to uncertainties in energy statistics. *Atmospheric Chemistry and*
631 *Physics*, 17(2), pp.1227-1239. DOI <https://doi.org/10.5194/acp-17-1227-2017>
632

633 IPCC, 2021: *Climate Change 2021: The Physical Science Basis. Contribution of Working Group I*
634 *to the Sixth Assessment Report of the Intergovernmental Panel on Climate Change*[Masson-
635 Delmotte, V., P. Zhai, A. Pirani, S.L. Connors, C. Péan, S. Berger, N. Caud, Y. Chen, L. Goldfarb,
636 M.I. Gomis, M. Huang, K. Leitzell, E. Lonnoy, J.B.R. Matthews, T.K. Maycock, T. Waterfield, O.
637 Yelekçi, R. Yu, and B. Zhou (eds.)]. Cambridge University Press, Cambridge, United Kingdom and
638 New York, NY, USA, In press, doi:[10.1017/9781009157896](https://doi.org/10.1017/9781009157896).

639

640 J. Muñoz-Sabater, Dutra, E., Agustí-Panareda, A., Albergel, C., Arduini, G., Balsamo, G.,
641 Boussetta, S., Choulga, M., Harrigan, S., Hersbach, H., Martens, B., Miralles, D. G., Piles, M.,
642 Rodríguez-Fernández, N. J., Zsoter, E., Buontempo, C., and Thépaut, J.-N.: ERA5-Land: A state-
643 of-the-art global reanalysis dataset for land applications, *Earth Syst. Sci. Data*,13, 4349–4383,
644 2021. <https://doi.org/10.5194/essd-13-4349-2021>.

645

646 Kochanov, R.V., Gordon, I.E., Rothman, L.S., Weislo, P., Hill, C. and Wilzewski, J.S., 2016.
647 HITRAN Application Programming Interface (HAPI): A comprehensive approach to working with
648 spectroscopic data. *Journal of Quantitative Spectroscopy and Radiative Transfer*, 177, pp.15-30.
649 DOI <https://doi.org/10.1016/j.jqsrt.2016.03.005>

650

651 Lin, X., van der A, R., de Laat, J., Eskes, H., Chevallier, F., Ciais, P., Deng, Z., Geng, Y., Song, X.,
652 Ni, X. and Huo, D., 2023. Monitoring and quantifying CO2 emissions of isolated power plants
653 from space. *EGUsphere*, pp.1-20. DOI <https://doi.org/10.5194/egusphere-2022-1490>

654

655 Loizzo, R., Guarini, R., Longo, F., Scopa, T., Formaro, R., Facchinetti, C. and Varacalli, G., 2018,
656 July. PRISMA: The Italian hyperspectral mission. In *IGARSS 2018-2018 IEEE International*
657 *Geoscience and Remote Sensing Symposium* (pp. 175-178). IEEE. DOI [https://doi.org/](https://doi.org/10.1109/IGARSS.2018.8518512)
658 [10.1109/IGARSS.2018.8518512](https://doi.org/10.1109/IGARSS.2018.8518512)

659

660 Nassar, R., Hill, T.G., McLinden, C.A., Wunch, D., Jones, D.B. and Crisp, D., 2017. Quantifying
661 CO₂ emissions from individual power plants from space. *Geophysical Research Letters*, 44(19),
662 pp.10-045. DOI <https://doi.org/10.1002/2017GL074702>
663

664 Nassar, R., Mastrogiacomo, J.P., Bateman-Hemphill, W., McCracken, C., MacDonald, C.G., Hill,
665 T., O'Dell, C.W., Kiel, M. and Crisp, D., 2021. Advances in quantifying power plant CO₂
666 emissions with OCO-2. *Remote Sensing of Environment*, 264, p.112579. DOI
667 <https://doi.org/10.1016/j.rse.2021.112579>
668

669 Nassar, R., Moeini, O., Mastrogiacomo, J.P., O'Dell, C.W., Nelson, R.R., Kiel, M., Chatterjee, A.,
670 Eldering, A. and Crisp, D., 2022. Tracking CO₂ emission reductions from space: A case study at
671 Europe's largest fossil fuel power plant. *Frontiers in Remote Sensing*, 3, p.98. DOI
672 <https://doi.org/10.3389/frsen.2022.1028240>
673

674 O'Dell, C.W., Connor, B., Bösch, H., O'Brien, D., Frankenberg, C., Castano, R., Christi, M.,
675 Eldering, D., Fisher, B., Gunson, M. and McDuffie, J., 2012. The ACOS CO₂ retrieval algorithm–
676 Part 1: Description and validation against synthetic observations. *Atmospheric Measurement*
677 *Techniques*, 5(1), pp.99-121. DOI <https://doi.org/10.5194/amt-5-99-2012>
678

679 O'Dell, C.W., Eldering, A., Wennberg, P.O., Crisp, D., Gunson, M.R., Fisher, B., Frankenberg, C.,
680 Kiel, M., Lindqvist, H., Mandrake, L. and Merrelli, A., 2018. Improved retrievals of carbon dioxide
681 from Orbiting Carbon Observatory-2 with the version 8 ACOS algorithm. *Atmospheric*
682 *Measurement Techniques*, 11(12), pp.6539-6576. DOI <https://doi.org/10.5194/amt-11-6539-2018>

683

684 Rodgers, C.D., 2000. *Inverse methods for atmospheric sounding: theory and practice* (Vol. 2).

685 World scientific.

686

687 Reuter, M., Buchwitz, M., Schneising, O., Krautwurst, S., O'Dell, C.W., Richter, A., Bovensmann,

688 H. and Burrows, J.P., 2019. Towards monitoring localized CO₂ emissions from space: co-located

689 regional CO₂ and NO₂ enhancements observed by the OCO-2 and S5P satellites. *Atmospheric*

690 *Chemistry and Physics*, 19(14), pp.9371-9383. DOI <https://doi.org/10.5194/acp-19-9371-2019>

691

692 Sierk, B., Bézy, J.L., Löscher, A. and Meijer, Y., 2019, July. The European CO₂ Monitoring

693 Mission: observing anthropogenic greenhouse gas emissions from space. In *International*

694 *Conference on Space Optics—ICSO 2018* (Vol. 11180, pp. 237-250). SPIE. DOI [https://doi.org/](https://doi.org/10.1117/12.2535941)

695 [10.1117/12.2535941](https://doi.org/10.1117/12.2535941)

696

697 Taylor, T.E., O'Dell, C.W., Baker, D., Bruegge, C., Chang, A., Chapsky, L., Chatterjee, A., Cheng,

698 C., Chevallier, F., Crisp, D. and Dang, L., 2023. Evaluating the consistency between OCO-2 and

699 OCO-3 XCO₂ estimates derived from the NASA ACOS version 10 retrieval

700 algorithm. *Atmospheric Measurement Techniques Discussions*, 2023, pp.1-61. DOI

701 <https://doi.org/10.5194/amt-16-3173-2023>

702

703 Thorpe, A.K., Frankenberg, C., Thompson, D.R., Duren, R.M., Aubrey, A.D., Bue, B.D., Green,

704 R.O., Gerilowski, K., Krings, T., Borchardt, J. and Kort, E.A., 2017. Airborne DOAS retrievals of

705 methane, carbon dioxide, and water vapor concentrations at high spatial resolution: application to

706 AVIRIS-NG. *Atmospheric Measurement Techniques*, 10(10), pp.3833-3850. DOI
707 <https://doi.org/10.5194/amt-10-3833-2017>
708
709 Van Geffen, J., Boersma, K.F., Eskes, H., Sneep, M., Ter Linden, M., Zara, M. and Veefkind, J.P.,
710 2020. S5P TROPOMI NO₂ slant column retrieval: Method, stability, uncertainties and comparisons
711 with OMI. *Atmospheric Measurement Techniques*, 13(3), pp.1315-1335. DOI
712 <https://doi.org/10.5194/amt-13-1315-2020>
713
714 Varon, D.J., Jacob, D.J., McKeever, J., Jervis, D., Durak, B.O., Xia, Y. and Huang, Y., 2018.
715 Quantifying methane point sources from fine-scale satellite observations of atmospheric methane
716 plumes. *Atmospheric Measurement Techniques*, 11(10), pp.5673-5686. DOI
717 <https://doi.org/10.5194/amt-11-5673-2018>